

[‡] Universidad Nacional de La Plata, La Plata, Argentina.

Fracture induced anisotropy in poroelastic media saturated by two-phase fluids

Juan E. Santos^{*†‡}

**Universidad de Buenos Aires, Facultad de Ingeniería, Instituto del Gas y del Petróleo,*

Av. Las Heras 2214 Piso 3 C1127AAR Buenos Aires, Argentina

Paseo del Bosque S/N, (1900) La Plata, Argentina

†Department of Mathematics, Purdue University,

150 N. University Street, West Lafayette, Indiana, 47907-2067, USA

(May 6, 2018)

Running head: **Anisotropy and two-phase fluids**

ABSTRACT

Wave induced fluid flow (WIFF) due to conversions from fast P-waves to slow diffusion-type P-waves at mesoscopic scale heterogeneities is a major cause of attenuation in fractured rocks. Reservoir rocks are saturated by multiphase fluids, and surface tensions induce relative motions between the nonwetting, wetting and solid phases, modifying the WIFF mechanism. To incorporate those effects I use a two-phase Biot model (2PBM) that includes saturation-dependent capillary pressure and relative permeabilities flow functions.

I use a finite element (FE) upscaling procedure to determine the stiffness components of a transversally isotropic viscoelastic (TIV) medium long-wave equivalent to an horizontally fractured poroelastic solid saturated by a two-phase fluid.

To determine the stiffness components of the TIV medium I use time-harmonic experi-

ments. Each experiment is associated with a boundary value problem (BVP) representing compressibility and shear experiments applied to a sample of the fractured Biot medium, and solved using the FE method.

To test the procedure, first I compare the results against a model valid for a fractured poroelastic solid saturated by a single-phase fluid (a SPBM) by using effective single-phase fluids. Finally, I applied the proposed methodology to the case of patchy saturation for two-phase gas-water and oil-water mixtures. The experiments show the necessity of using flow functions to obtain accurate estimates of attenuation and dispersion of qP and qSV waves in fractured hydrocarbon reservoir rocks.

INTRODUCTION

Hydrocarbon reservoirs are porous formations saturated for multiphase fluids. These formations present in many cases dense sets of aligned fractures (Gurevich, B., 2003; Gurevich, B. et al., 2009), which are very thin, compliant and highly permeable layers. Fractured hydrocarbon reservoirs have been the subject of interest in exploration and production geophysics, since generally, natural fractures control the permeability of the reservoir (Gurevich, B. et al., 2009).

The work presented by M. Biot in several classic papers (Biot, M.A., 1956a,b, 1962) give a model for wave propagation in a poroelastic solid saturated by a single-phase fluid. In what follows this model will be referred as the single-phase Biot model (SPBM), and predicts the existence of two compressional waves (P1 or fast wave and P2 or slow wave) and one shear wave. The P2 wave was first observed in laboratory by Plona (Plona, T., 1980) at ultrasonic frequencies.

One of the important mechanisms of seismic attenuation in fluid-saturated porous media is wave-induced fluid flow (WIFF), by which fast compressional (P) and shear (S) waves are converted to slow (diffusive) Biot waves at mesoscopic-scale (on the order of centimeters) heterogeneities (Carcione, J.M. and Picotti, S., 2006; Carcione, J.M., 2015).

White and coauthors (White, J.E. et al., 1975) and Dutta and Odé (Dutta, N.C. and Odé, H., 1979) analyzed the attenuation and dispersion of seismic waves in a brine saturated rock containing gas using models based on Biot's equations for single-phase fluids. Mochizuki (Mochizuki, S., 1982) studied experimental data in partially saturated rocks using Biot's theory. The fluids were modeled as a single phase one by means of a volume average for the density, an apparent viscosity and an effective fluid compressibility. Berryman and

coauthors (Berryman, J.G. et al., 1988) derived a model for wave propagation in porous rocks saturated by segregated fluids (liquid and gas) and for the case of mixing of liquid and gas.

The WIFF is particularly important in fractured poroelastic media. A planar fracture embedded in a fluid-saturated poroelastic background is a particular case of the thin layer problem, when one of the layers is very thin, highly permeable and compliant. A dense set of horizontal fractures in a fluid-saturated poroelastic medium behaves as a TIV medium when the average fracture distance is much smaller than the predominant wavelength of the traveling waves (Carcione, J.M., 2015).

For an analysis of anisotropy in stratified media, we mention the early work by Carcione and coauthors (Carcione, J. M. et al., 1991). Gelinsky and Shapiro (Gelinsky, S. and Shapiro, S. A., 1997) obtained the relaxed and unrelaxed stiffnesses of the equivalent poro-viscoelastic medium to a finely layered horizontally homogeneous material. Next, assuming that the layers are homogeneous and flow is perpendicular to the layering plane, Krzikalla and Müller (Krzikalla, F. and Müller, T. M., 2011) obtained the five complex and frequency-dependent stiffnesses of the equivalent transversely isotropic viscoelastic (TIV) medium. An analysis of anisotropy in fractured poroelastic media using the SPBM appeared in Carcione, J. M. et al. (2013).

Among works using numerical simulations to analyze dispersion, attenuation and anisotropy in Biot media we mention the work by Saenger and coauthors Saenger, E. H. et al. (2007), presenting numerical simulations in two-dimensional (2D) and three-dimensional (3D) media porous media saturated with fluids to analyze Biot's predictions in the high and low frequency limits of poroelasticity. Also, Grechka and Kachanov (Grechka, V. and Kachanov,

M., 2006) determined effective media corresponding to fractured rocks, performing 3D static FE simulations adding the individual contributions of the fractures and ignoring their interactions. Furthermore, the works by Wenzlau, F et al. (2010) and (Quintal, B. H. et al., 2011) use quasistatic FE modeling to analyze attenuation and dispersion effects associated with WIFF in poroelastic media.

The work by Santos J. E. and Carcione, J. M. (2015) presents a set of five harmonic compressibility and shear experiments to determine the stiffness coefficients and the corresponding energy velocities and dissipation factors of a long-wave equivalent TIV medium to a densely fractured SPBM. The experiments are formulated as boundary value problems (BVP) in the space-frequency domain that are solved using the finite element (FE) method.

Wave propagation theories and mesoscopic-loss effects considering two-phase fluids were presented by several authors. Auriault et al. (Auriault, J. L. and Lebaigue, O. and Bonnet, G. , 1989) used an homogenization theory and a description of the capillary effects at the pore scale, obtaining a generalized Darcy law. Lo et al. (Lo, W. C. et al., 2005) derived a model for waves traveling in an elastic porous solid permeated by two immiscible fluids incorporating both inertial and viscous drags in an Eulerian frame of reference, applying their model to a Columbia fine sandy loam saturated by air-water and oil-water. Qi, Q. et al. (2014) studied the effect of capillary pressure on the acoustic signature in the framework of the mesoscopic-loss theory. In this study the effect of capillarity was induced through the incorporation of a membrane stiffness in a random medium of patchy saturation.

To analyze the WIFF in a poroelastic solid saturated by a two-phase fluid using FE simulations, I generalize the time-harmonic experiments presented in (Santos J. E. and Carcione, J. M., 2015) using the model in (Santos, J. E. et al., 1990b,a; Ravazzoli, C.

L. et al., 2003), to be referred as a two-phase Biot model (2PBM). The 2PBM includes capillary forces in the constitutive relations and relative permeability functions defined in terms of two-phase Darcy's Law (Scheidegger, A. E., 1974; Peaceman, D. W., 1977). The 2PBM predicts the existence of two compressional (P) waves (one fast and two slow) and one shear (S) wave.

The first section of this paper we state the 2PBM describing the quasistatic behavior of a poroelastic solid saturated by a 2-phase fluid. The next section presents the time-harmonic BVP to determine the stiffness coefficients of TIV medium long-wave equivalent to a densely fractured poroelastic material saturated by a two-phase fluid. The last section presents first numerical experiments comparing the analytical results with those obtained using the 2PBM, and finally shows the application of the procedure to the case of patchy gas-brine and oil-brine patchy saturation.

THE 2PBM DESCRIBING A POROELASTIC SOLID SATURATED BY A TWO-PHASE FLUID

We consider a porous solid saturated by two immiscible fluids, where we distinguish a *wetting* phase and a *nonwetting* one, to be denoted with the subscripts (or superscripts) “*w*” and “*n*”, respectively. Let $\mathbf{x} = (x, y, z)$ and $S_w = S_w(\mathbf{x})$ and $S_n = S_n(\mathbf{x})$ denote the wetting and nonwetting fluid saturations averaged over the bulk material, respectively, with S_{rw} and S_{rn} being the corresponding residual saturations. We assume that both fluid phases completely saturate the porous part and move within the pore space, (Peaceman, D. W., 1977; Scheidegger, A. E., 1974), so that $S_w + S_n = 1$. and $S_{rn} < S_n < 1 - S_{rw}$.

Denote by $\mathbf{u}^s = (u_i^s)$, $\tilde{\mathbf{u}}^n = (\tilde{u}_i^n)$ and $\tilde{\mathbf{u}}^w = (\tilde{u}_i^w)$, $i = 1, 2, 3$ the time Fourier transforms of

the averaged displacement vectors of the solid, nonwetting and wetting phases, respectively, and let $\phi = \phi(\mathbf{x})$ denote the matrix effective porosity. The relative fluid displacements are

$$\mathbf{u}^\theta = \phi(\tilde{\mathbf{u}}^\theta - \mathbf{u}^s), \quad \xi^\theta = -\nabla \cdot \mathbf{u}^\theta, \quad \theta = n, w.$$

Let $\varepsilon_{ij}(\mathbf{u}^s)$ and $e^s = \varepsilon_{ii}(\mathbf{u}^s)$ be the Fourier transforms of the strain tensor of the solid and its linear invariant, respectively. Also, set $\mathbf{u} = (\mathbf{u}^s, \mathbf{u}^n, \mathbf{u}^w)$.

Let $\tau = \tau_{ij}$ and $\varepsilon = \varepsilon_{ij}$, $i, j = 1, 2, 3$ denote the Fourier transforms infinitesimal changes in the stress and strain tensors, respectively. Also, let P_n and P_w denote the Fourier transforms of the infinitesimal changes in the nonwetting and wetting fluid pressures, respectively. These infinitesimal changes are taken with respect to corresponding reference values $\bar{\tau}_{ij}$, \bar{P}_n , and \bar{P}_w associated with the initial equilibrium state with associated nonwetting fluid saturation \bar{S}_n and porosity $\bar{\phi}$.

P_n and P_w are related through the capillary relation (Peaceman, D. W., 1977; Scheidter, A. E., 1974; Santos, J. E. et al., 1990b)

$$P_{ca} = P_{ca}(S_n + \bar{S}_n) = \bar{P}_n + P_n - (\bar{P}_w + P_w) = P_{ca}(\bar{S}_n) + P_n - P_w \geq 0. \quad (1)$$

Ignoring hysteresis, P_{ca} is a positive and strictly increasing function of the nonwetting fluid saturation.

The stress-strain of a 2PBM are (Santos, J. E. et al., 1990b; Ravazzoli, C. L. et al., 2003):

$$\tau_{ij}(\mathbf{u}) = 2\mu \varepsilon_{ij} + \delta_{ij}(\lambda_c e^s - B_1 \xi^n - B_2 \xi^w), \quad (2)$$

$$\mathcal{T}_n(\mathbf{u}) = (\bar{S}_n + \beta + \zeta) P_n - (\beta + \zeta) P_w = -B_1 e^s + M_1 \xi^n + M_3 \xi^w, \quad (3)$$

$$\mathcal{T}_w(\mathbf{u}) = (\bar{S}_w + \zeta) P_w - \zeta P_n = -B_2 e^s + M_3 \xi^n + M_2 \xi^w, \quad (4)$$

where

$$\beta = \frac{P_{ca}(\bar{S}_n)}{P'_{ca}(\bar{S}_n)}, \zeta = \frac{\bar{P}_w}{P'_{ca}(\bar{S}_n)}. \quad (5)$$

The quantities τ_{ij} , \mathcal{T}_n and \mathcal{T}_w are the generalized forces of the system. The coefficient μ is the shear modulus of the dry rock (i.e, $\mu = \mu_m$), while $\lambda_c = K_c - \frac{2}{3}\mu$ with K_c being the undrained bulk modulus. The other coefficients in (2)-(4) can be determined as indicated in Santos, J. E. et al. (1990b); Ravazzoli, C. L. et al. (2003).

The equations for a 2PBM in the diffusive range of frequencies, stated in the space–frequency domain are Santos, J. E. et al. (1990b); Ravazzoli, C. L. et al. (2003):

$$\nabla \cdot \boldsymbol{\tau}(\mathbf{u}) = 0, \quad (6)$$

$$i\omega d_n \mathbf{u}^n - i\omega d_{nw} \mathbf{u}^w + \nabla \mathcal{T}_n(\mathbf{u}) = 0, \quad (7)$$

$$i\omega d_w \mathbf{u}^w - i\omega d_{nw} \mathbf{u}^n + \nabla \mathcal{T}_w(\mathbf{u}) = 0. \quad (8)$$

The coefficients d_n , d_w and d_{nw} are taken to be of the form:

$$d_l(\bar{S}_l) = (\bar{S}_l)^2 \frac{\eta_l}{\kappa K_{rl}(\bar{S}_l)}, \quad l = n, w, \quad (9)$$

$$d_{r,nw}(\bar{S}_n, \bar{S}_w) = \epsilon (d_n(\bar{S}_n) d_w(\bar{S}_w)). \quad (10)$$

Here η_n, η_w are the fluid viscosities and κ , $K_{rn}(S_n)$, $K_{rw}(S_w)$ are the absolute permeability and the relative permeability functions, respectively, while $d_{r,nw}(S_n, S_w)$ is a cross dissipative function. In the numerical experiments we choose $\epsilon = 0.01$.

THE EQUIVALENT TIV MEDIUM

Let us consider x_1 and x_3 as the horizontal and vertical coordinates, respectively. As shown by Krzikalla, F. and Müller, T. M. (2011) a fluid-saturated poroelastic solid with a dense

set of horizontal fractures behaves as a TIV medium with a vertical symmetry axis at long wavelengths.

Denote by $\tau_{ij}(\tilde{\mathbf{u}}_s)$ and $\epsilon_{ij}(\tilde{\mathbf{u}}_s)$ the stress and strain tensor components of the equivalent TIV medium, where $\tilde{\mathbf{u}}_s$ denotes the solid displacement vector at the macroscale. The corresponding stress-strain relations, stated in the space-frequency domain and assuming a closed system are (Carcione, J. M., 1992; Carcione, J.M., 2015)

$$\tau_{11}(\tilde{\mathbf{u}}_s) = p_{11} \epsilon_{11}(\tilde{\mathbf{u}}_s) + p_{12} \epsilon_{22}(\tilde{\mathbf{u}}_s) + p_{13} \epsilon_{33}(\tilde{\mathbf{u}}_s), \quad (11)$$

$$\tau_{22}(\tilde{\mathbf{u}}_s) = p_{12} \epsilon_{11}(\tilde{\mathbf{u}}_s) + p_{11} \epsilon_{22}(\tilde{\mathbf{u}}_s) + p_{13} \epsilon_{33}(\tilde{\mathbf{u}}_s), \quad (12)$$

$$\tau_{33}(\tilde{\mathbf{u}}_s) = p_{13} \epsilon_{11}(\tilde{\mathbf{u}}_s) + p_{13} \epsilon_{22}(\tilde{\mathbf{u}}_s) + p_{33} \epsilon_{33}(\tilde{\mathbf{u}}_s), \quad (13)$$

$$\tau_{23}(\tilde{\mathbf{u}}_s) = 2 p_{55} \epsilon_{23}(\tilde{\mathbf{u}}_s), \quad (14)$$

$$\tau_{13}(\tilde{\mathbf{u}}_s) = 2 p_{55} \epsilon_{13}(\tilde{\mathbf{u}}_s), \quad (15)$$

$$\tau_{12}(\tilde{\mathbf{u}}_s) = 2 p_{66} \epsilon_{12}(\tilde{\mathbf{u}}_s). \quad (16)$$

Note that in a TIV medium $p_{12} = p_{11} - 2 p_{66}$, so that only five independent stiffness, i.e., $p_{11}, p_{33}, p_{13}, p_{55}$ and p_{66} need to be considered.

As shown in Santos J. E. and Carcione, J. M. (2015) these stiffnesses can be determined using five time-harmonic experiments. Next we present the generalization of those experiments using the 2PBM to represent a fractured poroelastic solid saturated by a two-phase fluid. We will solve (6)-(8) in the 2D case on a reference square $\Omega = (0, L)^2$ with boundary Γ in the (x_1, x_3) -plane.

Set $\Gamma = \Gamma^L \cup \Gamma^B \cup \Gamma^R \cup \Gamma^T$, where $\Gamma^L, \Gamma^R, \Gamma^B$ and Γ^T denote the left, right, bottom and top boundaries of Ω . Denote by $\boldsymbol{\nu}$ the unit outer normal on Γ and let $\boldsymbol{\chi}$ be a unit tangent on Γ oriented counterclockwise so that $\{\boldsymbol{\nu}, \boldsymbol{\chi}\}$ is an orthonormal system on Γ . To

determine the five independent stiffness coefficients, we solve (6)-(8) in Ω with the boundary conditions

$$\mathbf{u}^n \cdot \boldsymbol{\nu} = 0, \quad \mathbf{u}^w \cdot \boldsymbol{\nu} = (x_1, x_3) \in \Gamma, \quad (17)$$

i.e., no fluids enter or leave the sample, and the additional boundary conditions:

for p_{33} :

$$\boldsymbol{\tau}(\mathbf{u})\boldsymbol{\nu} \cdot \boldsymbol{\nu} = -\Delta P, \quad (x_1, x_3) \in \Gamma^T, \quad (18)$$

$$\boldsymbol{\tau}(\mathbf{u})\boldsymbol{\nu} \cdot \boldsymbol{\chi} = 0, \quad (x_1, x_3) \in \Gamma, \quad (19)$$

$$\mathbf{u}^s \cdot \boldsymbol{\nu} = 0, \quad (x_1, x_3) \in \Gamma \setminus \Gamma^T. \quad (20)$$

Using the relation

$$\frac{\Delta V(\omega)}{V} = -\frac{\Delta P}{p_{33}(\omega)}, \quad (21)$$

where V the original volume of the sample, $p_{33}(\omega)$ can be determined from (21) measuring the volume change $\Delta V(\omega) \approx Lu_{s,3}^{(33,T)}(\omega)$, where $u_{s,3}^{(33,T)}(\omega)$ is the average of the vertical component of the solid phase at the boundary Γ^T .

for p_{11} :

$$\boldsymbol{\tau}(\mathbf{u})\boldsymbol{\nu} \cdot \boldsymbol{\nu} = -\Delta P, \quad (x_1, x_3) \in \Gamma^R, \quad (22)$$

$$\boldsymbol{\tau}(\mathbf{u})\boldsymbol{\nu} \cdot \boldsymbol{\chi} = 0, \quad (x_1, x_3) \in \Gamma, \quad (23)$$

$$\mathbf{u}^s \cdot \boldsymbol{\nu} = 0, \quad (x_1, x_3) \in \Gamma \setminus \Gamma^R. \quad (24)$$

Thus, this experiment determines p_{11} as indicated for p_{33} , measuring the oscillatory volume change.

for p_{13} :

$$\boldsymbol{\tau}(\mathbf{u})\boldsymbol{\nu} \cdot \boldsymbol{\nu} = -\Delta P, \quad (x_1, x_3) \in \Gamma^R \cup \Gamma^T, \quad (25)$$

$$\boldsymbol{\tau}(\mathbf{u})\boldsymbol{\nu} \cdot \boldsymbol{\chi} = 0, \quad (x_1, x_3) \in \Gamma, \quad (26)$$

$$\mathbf{u}^s \cdot \boldsymbol{\nu} = 0, \quad (x_1, x_3) \in \Gamma^L \cup \Gamma^B. \quad (27)$$

From (11) and (13) we get

$$\sigma_{11} = p_{11}\epsilon_{11} + p_{13}\epsilon_{33} \quad \sigma_{33} = p_{13}\epsilon_{11} + p_{33}\epsilon_{33},$$

with ϵ_{11} and ϵ_{33} being the (macroscale) strain components at Γ^L and Γ^T , respectively. Since

$\sigma_{11} = \sigma_{33} = -\Delta P$ (c.f.(25)) we obtain $p_{13}(\omega)$ as

$$p_{13}(\omega) = \frac{p_{11}\epsilon_{11} - p_{33}\epsilon_{33}}{\epsilon_{11} - \epsilon_{33}}. \quad (28)$$

for p_{55} :

$$-\boldsymbol{\tau}(\mathbf{u})\boldsymbol{\nu} = \mathbf{g}, \quad (x_1, x_3) \in \Gamma^T \cup \Gamma^L \cup \Gamma^R, \quad (29)$$

$$\mathbf{u}_s = 0, \quad (x_1, x_3) \in \Gamma^B, \quad (30)$$

where

$$\mathbf{g} = \begin{cases} (0, \Delta G), & (x_1, x_3) \in \Gamma^L, \\ (0, -\Delta G), & (x_1, x_3) \in \Gamma^R, \\ (-\Delta G, 0), & (x_1, x_3) \in \Gamma^T. \end{cases}$$

The change in shape of the rock sample allows to obtain $p_{55}(\omega)$ by using the relation

$$\text{tg}(\beta(\omega)) = \frac{\Delta G}{p_{55}(\omega)}, \quad (31)$$

where $\beta(\omega)$ is the departure angle between the original positions of the lateral boundaries and those after applying the shear stresses, that can be determined by measuring the average horizontal displacement at Γ^T (Santos J. E. and Carcione, J. M., 2015).

for p_{66} :

$$-\boldsymbol{\tau}(\mathbf{u})\boldsymbol{\nu} = \mathbf{g}_2, \quad (x_1, x_2) \in \Gamma^B \cup \Gamma^R \cup \Gamma^T, \quad (32)$$

$$\mathbf{u}_s = 0, \quad (x_1, x_2) \in \Gamma^L, \quad (33)$$

where

$$\mathbf{g}_2 = \begin{cases} (\Delta G, 0), & (x_1, x_2) \in \Gamma^B, \\ (-\Delta G, 0), & (x_1, x_2) \in \Gamma^T, \\ (0, -\Delta G), & (x_1, x_2) \in \Gamma^R. \end{cases}$$

Then, we proceed as indicated for $p_{55}(\omega)$.

The approximate solution of these five BVP was computed using a FE procedure. We used bilinear functions to approximate each component of the solid displacement vector, while for the nonwetting and wetting fluid displacements we used a closed subspace of the vector part of the Raviart-Thomas-Nedelec space of zero order Raviart, P.A. and Thomas, J.M. (1975). See (Santos J. E. and Carcione, J. M., 2015) for details on the description of these FE spaces. Also, in the work by Santos J. E. and Carcione, J. M. (2015) it is shown that the error associated with these finite-element problems, measured in the energy norm, is on the order of $O(h^{1/2})$, with h being the size of the computational mesh. The proof can be generalized to the case of two-phase fluids analyzed here.

NUMERICAL EXPERIMENTS

The FE procedures described above were implemented to determine the five complex stiffnesses $p_{IJ}(\omega)$ as a function of frequency and the corresponding phase velocities and dissipation coefficients. In all the experiments the numerical samples were discretized using

a 80×80 uniform mesh representing 8 periods of 9 cm background sandstone and 1 cm fracture thickness. Also, we chose $\overline{P}_w = 0$ in (5). Both background and fractures have grain density $\rho_s = 2650 \text{ kg/m}^3$, and bulk modulus $K_s = 37 \text{ GPa}$. Porosity and permeability are $\phi = 0.25$, $\kappa = 1 \text{ D}$ in the background and $\phi = 0.5$, $\kappa = 4.44 \text{ D}$ in the fractures. The dry bulk and shear moduli are $K_m = 4.8 \text{ GPa}$, $\mu = 5.7 \text{ GPa}$ in the background and $K_m = 0.58 \text{ GPa}$, $\mu = 0.68 \text{ GPa}$ in the fractures.

The saturant fluids were chosen to be two-phase mixtures of gas-brine or oil-brine, with brine being the wetting phase. The bulk modulus, density and viscosity of the fluids are 2.25 GPa, 1040 kg/m³ and 0.03 Pa·s for brine, 0.012 GPa, 78 Kg/m³ and 0.00015 Pa·s for gas and 0.57 GPa, 700 Kg/m³ and 0.01 Pa·s for oil, respectively.

The two-phase fluid is described in terms of relative permeabilities, $K_{rn}(S_n)$, $K_{rw}(S_n)$, and capillary pressure function, $P_{ca}(S_n)$, taken to be (Douglas, J., Jr. et al., 1997; Ravazzoli, C. L. et al., 2003):

$$\begin{aligned} K_{rn}(S_n) &= (1 - (1 - S_n)/(1 - S_{rn}))^2, \\ K_{rw}(S_n) &= ([1 - S_n - S_{rw}] / (1 - S_{rw}))^2, \\ P_{ca}(S_n) &= A \left(1/(S_n + S_{rw} - 1)^2 - S_{rn}^2/[S_n(1 - S_{rn} - S_{rw})]^2 \right), \end{aligned}$$

where A is the capillary pressure amplitude, chosen to be 30 kPa in all experiments. These relations are based on laboratory experiments performed on different porous rocks during imbibition and drainage processes (neglecting hysteresis effects) and are of common use in multiphase flow reservoir simulation.

The first experiment compares energy velocities and attenuation coefficients of qP, qSV, and SH waves for a two-phase gas-water mixture defined using the 2PBM with those the corresponding to the analytical solution using the SPBM as in Krzikalla, F. and Müller, T.

M. (2011), with the single-phase fluid determined by weighting the gas and water properties with the corresponding saturations in background and fractures. To simulate almost full brine saturation in the background and almost full gas saturation in the fractures, residual saturations are chosen to be $S_{rn} = 0, S_{rw} = 0.01$, with $S_n = 0.0012$ in the background and $S_n = 0.998$ in the fractures.

Figures 1 and 2 display polar plots of the energy velocities and attenuation coefficients of qP and qSV waves for the 2PBM at 50 Hz as functions of the propagation angle and those the corresponding to the analytical solution using the SPBM. In all Figures 0 and 90 degrees correspond to waves arriving parallel and normal to the fracture layering, respectively.

It can be seen in Figure 1 that both qP and qSV waves exhibit velocity anisotropy for both the analytical solution and the 2PBM. Also, qP waves have different anisotropic behavior, i.e., for waves traveling normally to the fracture layering the analytical model predicts faster velocities than the 2PBM, while the opposite is predicted for qP waves traveling parallel to the fracture plane. Besides, qSV velocities exhibit quite similar anisotropy for both models.

Figure 2 show that qP waves atenuation is higher parallel than nornal to the fractures, an it is much higher for the 2PBM than for the analytical solution for all angles. Furthermore, the 2PBM predicts attenuation for qSV waves, while they are almost lossless for the analytical solution, with their values shown as a point at the origin. These differences in attenuation coefficients are due to the combined effect of capillary pressure and relative permeability functions.

To analyze the behavior of the attenuation coefficient predicted by the 2PBM for qP waves it is convenient to analyze the L^2 -norms of the gradients of the fluid pressures $\tilde{\mathcal{T}}$ and

of the relative nonwetting and wetting fluid displacements for the p_{11} and p_{33} experiments, respectively. For this purpose let us define the total fluid pressure in the 2PBM as $\tilde{\mathcal{T}} = \mathcal{T}^n + \mathcal{T}^w$, with \mathcal{T}^n and \mathcal{T}^w being the generalized forces defined in (3) and (4), respectively. Next, with $\|f\|_0$ denoting the L^2 norm of the function f , let us define the following quantities:

$$\|\nabla \tilde{\mathcal{T}}\|_{\{0,II\}}, \quad R_{II}^{n,w} = \frac{\|u_I^n\|_{\{0,II\}}}{\|u_I^w\|_{\{0,II\}}}, \quad , I = 1, 3. \quad (34)$$

In (34) the subindices $I, \{0, II\}$ indicate the experiments to determine the stiffness p_{II} , $I = 1, 3$, respectively.

We obtained $\|\nabla \tilde{\mathcal{T}}\|_{\{0,11\}} \approx 0.9Pa$, $\|\nabla \tilde{\mathcal{T}}\|_{\{0,33\}} \approx 0.6Pa$, $R_{11}^{n,w} \approx 3.07$, $R_{33}^{n,w} \approx 3.45$, so that the gas and brine phases have displacements of the same order of magnitude, and consequently dissipation due to the motions of the two fluid phases are similar for the directions parallel and normal to the fracture layering. But gradients of pressure are 50 % larger for parallel than for normal compressions to the fracture layering, explaining the behavior of the attenuation coefficient for qP waves seen in Figure 2.

Figure 3 shows polar plots of energy velocities of SH waves. They exhibit velocity anisotropy for both models, but with different behavior, with SH waves traveling faster for the analytical solution than for the 2PBM when moving normally to the fracture plane. The opposite behavior is seen in the horizontal plane.

Figures 4 and 5 display phase velocities and attenuation coefficients for the 2PBM and the analytical solution as function of frequency in the range 1 Hz- 1 kHz for waves parallel (“11” waves) and normal (“33” waves) to the fracture layering. The two-phase fluid is a water-gas mixture with the same residual saturations and gas saturations in background and fractures as in Figures 1, 2 and 3. Attenuation coefficients and phase velocities in Figures 4 and 5 are denoted Q11, vp11, Q33, vp33 for “11” and “33” waves, respectively

Figure 4 shows that energy velocities for the analytical model and those computed using the harmonic experiments for the 2PBM are in perfect agreement. Figure 5 shows that attenuation values of the analytical solution and the harmonic 2PBM have attenuation peaks above 100 Hz for both “11” and “33” waves. For the 2PBM the attenuation peaks for “11” and “33” waves move to lower frequencies.

Next note that in a realistic brine-wet poroelastic sample saturated by a two-phase gas-brine mixture there exists always a certain percentage of immobile brine, measured by the value of the residual water saturation S_{rw} . Thus in all the remaining experiments residual saturations will be chosen to be $S_{rn} = 0.$, $S_{rw} = 0.1$.

Figures 6 and 7 displays polar plots of energy velocities and attenuation coefficients at 50 Hz for qP and qSV waves for the 2PBM as function of the propagation angle and those of the analytical solution using effective single-phase fluids. The two-phase fluid is a gas-water mixture with gas saturation $S_n = 0.012$ in the background and $S_n = 0.898$ in the fractures.

Energy velocities of qP and qSV waves in Figure 6 show the same behavior than in Figure 1, i.e, their anisotropic behavior are little affected by changes in residual saturations and saturation values of the fluid phases.

Figure 7 display a strong change in attenuation of qP waves. For the 2PBM they are highly attenuated when traveling close to the direction normal to the fracture plane, and are almost not attenuated when moving parallel to such plane. For the analytical solution, qP waves are more attenuated when traveling parallel to the fractures, with twice the attenuation suffered when moving parallel to that plane. Besides, Figure 7 shows that the 2PBM predicts qSV waves suffering attenuation, while they are almost lossless for the analytical solution. Also notice that attenuation of qSV waves is smaller in Figure 7 than

in Figure 2, indicating that qSV attenuation is sensitive to changes in residual saturations.

The behavior of the attenuation coefficients of qP waves in Figure 7 can be analyzed as it was done for Figure 2 by computing the norms of the nonwetting and wetting fluid displacements and the gradients of the total fluid pressure $\tilde{\mathcal{T}}$. In this experiment we have $\|\nabla\tilde{\mathcal{T}}\|_{\{0,11\}} \approx 3.5Pa$, $\|\nabla\tilde{\mathcal{T}}\|_{\{0,33\}} \approx 0.9Pa$, $R_{11}^{n,w} = 22.6$, $R_{33}^{n,w} = 58.4$. In this experiment the displacements of the the gas and brine phase are quite different, being more than one order of magnitude different for directions normal to the fractures than for parallel to such direction (about 160 % larger when measured in the L^2 norm). Thus in this experiment the difference in the displacements of both phases is the cause of the attenuation behavior of qP waves as seen in Figure 7, independently of the fact that gradients of pressure may indicate the opposite behavior, as seen in the curve for the analytical solution.

This quite different behavior in attenuation of qP waves for the 2PBM as compared with the analytical solution (that *does not* take into account the different displacements of the two fluid phases), is due to the combined effects of residual saturations, capillary pressure and relative permeability functions.

The case of patchy saturation

Patchy saturation occurs in hydrocarbon reservoirs at gas-brine or oil-brine contact. Patchy-saturation patterns induce important mesoscopic-loss effects at the seismic band of frequencies, as was first as shown by (White, J.E. et al., 1975).

Figure 8 shows the spatial distribution of the two-phase fluid in the form of patches of nonwetting saturation values $S_n = 0.012$, $S_n = 0.2$ and $S_n = 0.898$, with overlall nonwetting fluid saturation 10 %. The work by Santos J. E. and Carcione, J. M. (2015) explains how

to generate this type of stochastic fractal distributions.

Figures 9, 10, 11 and 12 display energy velocities and attenuation coefficients of qP and qSV waves for the 2PBM and two-phase gas-brine or oil-brine fluid mixtures with residual saturations $S_{rn} = 0, S_{rw} = 0.1$ for the following Cases:

- Case 1: Background and fractures are saturated with a gas-brine mixture, background has gas saturation $S_n = 0.012$, fractures have gas saturation $S_n = 0.898$.
- Case 2: Background and fractures are saturated with patches of a gas-brine mixture. Patches have gas saturation $S_n = 0.012, 0.2$ and 0.898 . Overall gas saturation is 10 %.
- Case 3: Background and fractures are saturated with a oil-brine mixture, background has oil saturation $S_n = 0.012$, fractures have oil saturation $S_n = 0.898$
- Case 4: Background and fractures are saturated with patches of an oil-brine mixture, Patches have oil saturation $S_n = 0.012, 0.2$ and 0.898 . Overall oil saturation is 10 %.

The labels “fractures with gas” “and fractures with oil” in Figures 9, 10, 11 and 12 correspond to the nonwetting saturations in Cases 1 and 3.

Figure 9 shows velocity anisotropy for all cases, and for Cases 1 and 2 velocities are always lower for Case 2 (patchy saturation). Instead, for Cases 3 and 4, velocities coincide for angles up to 30 degrees and then increase until attaining a maximum value at normal incidence to the fracture layering.

Figure 10 shows a noticeable increase in attenuation of qP waves when patches of the nonwetting fluid (gas or oil) are present. For the patchy Cases 2 and 4, attenuation coefficients can be analyzed as was done before for Figures 2 and 7 by computing the L^2

norm of gradients of pressure and the quotients of L^2 norms of nonwetting and wetting phases associated with the p_{11} and p_{33} experiments. For Case 2 (patchy gas-brine) we have $\|\nabla\tilde{\mathcal{T}}\|_{\{0,11\}} \approx 1.41Pa$, $\|\nabla\tilde{\mathcal{T}}\|_{\{0,33\}} \approx 2.9Pa$, $R_{11}^{n,w} \approx 3.41$, $R_{33}^{n,w} \approx 3.156$. Thus we have similar attenuation due to differences in displacements of the nonwetting and wetting phases, but gradients of pressure are about 42 % larger for normal than for parallel directions to the fracture layering, explaining the behavior of the attenuation coefficients for qP waves seen in Figure 10. The analysis of values of L^2 norms for patchy oil-brine allow to have the same conclusion about attenuation of qP waves in Case 4.

Besides, the higher attenuation of qP waves seen in Figure 10 for Case 4 (patchy oil-brine) as compared with Case 2 (patchy gas-brine), can be explained by the much larger gradients of the total fluid pressure $\tilde{\mathcal{T}}$ for Case 4 than for Case 2, with maximum values of 47 Pa/m and 27 Pa/m, respectively, for compressions normal to the fractures. This effect is illustrated in Figures 13 and 14 displaying gradients of the total fluid pressure at 50 Hz for these two Cases.

Figure 11 shows energy velocity anisotropy for qSV waves, with decreasing values for patchy saturation (Cases 2 and 4), with respect to the non-patchy Cases 1 and 3.

Besides, Figure 12 shows that for angles close to 45 degrees, qSV waves suffer attenuation, with decreasing attenuation values for Cases 2 and 4 with respect to Cases 1 and 3.

CONCLUSIONS

I proposed the use of a model that includes capillary pressure and relative permeability flow functions to analyze the WIFF and mesoscopic loss effects when fractured poroelastic rocks

are saturated by two-phase fluids.

By extending the known upscaling finite element procedures for fractured poroelastic rocks saturated by single-phase fluids, I observed that energy velocities and attenuation coefficients suffer significant changes with respect to effective single-phase fluids when using a proper representation of two-phase fluids using flow functions, which are of common use in numerical reservoir simulations.

One important observation is that attenuation behavior of qP waves is determined by the combined effect of the gradients of both fluid pressures and differences between the displacements of the two fluid phases, the latter being a new energy dissipation effect not present for single-phase fluids. Furthermore, velocity anisotropy for qP and qSV shows different behavior for two-phase and effective single-phase fluids.

Thus, the finite element procedure here presented and analyzed allows to determine a more accurate VTI medium long wave equivalent to a poroelastic solid saturated by a two-phase fluid, with application to wave propagation analysis and modeling in hydrocarbon reservoirs.

REFERENCES

- Auriault, J. L. and Lebaigue, O. and Bonnet, G. , 1989, Dynamics of two immiscible fluids flowing through deformable porous media: *Transport in Porous Media*, **4**, 105–128.
- Berryman, J.G., Thigpen, L., and Chin, R., 1988, Bulk elastic wave propagation in partially saturated porous solids: *J. Acoust. Soc. Am.*, **84**, 360–373.
- Biot, M.A., 1956a, Theory of propagation of elastic waves in a fluid-saturated porous solid. i. low frequency range: *J. Acoust. Soc. Am.*, **28**, 168–171.
- , 1956b, Theory of propagation of elastic waves in a fluid-saturated porous solid. ii. high frequency range: *J. Acoust. Soc. Am.*, **28**, 179–191.
- , 1962, Mechanics of deformation and acoustic propagation in porous media: *Journal of Applied Physics*, **33**, 1482–1498.
- Carcione, J. M., 1992, Anisotropic q and velocity dispersion of finely layered media: *Geophys. Prosp.*, **40**, 761–783.
- Carcione, J. M., Gurevich, B, Santos, J. E., and Picotti, S., 2013, Angular and frequency dependent wave velocity and attenuation in fractured porous media: *Pure and Applied Geophysics*, **170**, 1673–1683.
- Carcione, J. M., Kosloff, D., and Behle, A., 1991, Long wave anisotropy in stratified media: a numerical test: *Geophysics*, **56**, 245–254.
- Carcione, J.M., 2015, *Fields in real media. theory and numerical simulation of wave propagation in anisotropic, anelastic, porous and electromagnetic media*: Elsevier. (Third edition, extended and revised), Oxford.
- Carcione, J.M. and Picotti, S., 2006, P-wave seismic attenuation by slow-wave diffusion: Effects of inhomogeneous rock properties: *Geophysics*, **71 No3**, O1–O8.
- Douglas, J., Jr., Furtado, F., and Pereira, F., 1997, On the numerical simulation of water-

- flooding of heterogeneous petroleum reservoirs: *Comput. Geosci.*, **1**, 155–190.
- Dutta, N.C. and Odé, H., 1979, Attenuation and dispersion of compressional waves in fluid-filled porous rocks with partial gas saturation (white model). part i: Biot theory: *Geophysics*, **44 No 11**, 1777–1788.
- Gelinsky, S. and Shapiro, S. A., 1997, Poroelastic Backus-averaging for anisotropic, layered fluid and gas saturated sediments: *Geophysics*, **62**, 1867–1878.
- Grechka, V. and Kachanov, M., 2006, Effective elasticity of rocks with closely spaced and intersecting cracks: *Geophysics*, **71**, D85–D91.
- Gurevich, B., 2003, Elastic properties of saturated porous rocks with aligned fractures: *Journal of Applied Geophysics*, **54**, 203–218.
- Gurevich, B., Brajanovski, M., Galvin, R. J., Müller, T. M., and Toms-Stewart, J., 2009, P-wave dispersion and attenuation in fractured and porous reservoirs—poroelasticity approach: *Geophysical Prospecting*, **57**, 225–237.
- Krzikalla, F. and Müller, T. M., 2011, Anisotropic P-SV-wave dispersion and attenuation due to interlayer flow in thinly layered porous rocks: *Geophysics*, **76**, WA135.
- Lo, W. C., Sposito, G. , and Majer, E. , 2005, Wave propagation through elastic porous media containing two immiscible fluids: *Water Resources Research*, **41**, W02025, 1–20.
- Mochizuki, S., 1982, Attenuation in partially saturated rocks: *J. of Geophys. Res.*, **87**, 8598–8604.
- Peaceman, D. W., 1977, *Fundamentals of numerical reservoir simulation*: Elsevier.
- Plona, T., 1980, Observation of a second bulk compressional wave in a porous medium at ultrasonic frequencies: *Applied Physics Letters*, **36**, 259–261.
- Qi, Q., Müller, T. M., Gurevich, B., Lopes, S., Lebedev, M., and Caspari, E., 2014, Quantifying the effect of capillarity on attenuation and dispersion in patchy-saturated rocks:

- Geophysics, **79**, WB35WB50.
- Quintal, B. H., Steeb, M., Frehner, M., and Schmalholz, S. M., 2011, Quasi-static finite element modeling of seismic attenuation, and dispersion due to wave-induced fluid flow in poroelastic media: J. Geophys. Research, **116**, B01201.
- Ravazzoli, C. L., Santos, J. E., and Carcione, J. M., 2003, Acoustic and mechanical response of reservoir rocks under variable saturation and effective pressure: J. Acoust. Soc. Am., **13**, 1801–1811.
- Raviart, P.A. and Thomas, J.M., 1975, Mixed finite element method for 2^{nd} order elliptic problems: Mathematical aspects of the finite element methods, lecture notes of mathematics, vol. 606: Springer.
- Saenger, E. H., Ciz, R., Krüger, O. S., Schmalholz, S. M., Gurevich, B, and Shapiro, S. A., 2007, Finite-difference modeling of wave propagation on microscale: A snapshot of the work in progress: Geophysics, **72**, SM293–SM300.
- Santos J. E. and Carcione, J. M., 2015, Finite-element harmonic experiments to model fractured induced anisotropy in poroelastic media: Comput. Methods Appl. Mech. Engrg., **283**, 1189–1213.
- Santos, J. E., Corberó, J., and Douglas, J., Jr., 1990a, Static and dynamic behaviour of a porous solid saturated by a two-phase fluid: J. Acoust. Soc. Am., **87**, 1428–1438.
- Santos, J. E., Douglas, J., Jr., Corberó, J., and Lovera, O. M., 1990b, A model for wave propagation in a porous medium saturated by a two-phase fluid: J. Acoust. Soc. Am., **87**, 1439–1448.
- Scheidegger, A. E., 1974, The physics of flow through porous media: University of Toronto, Toronto.
- Wenzlau, F, Altmann, J. B., and Müller, T., 2010, Anisotropic dispersion and attenuation

due to wave-induced flow: quasi-static finite element modeling in poroelastic solids: J. Geophys. Res., **115**, B07204.

White, J.E., Mikhaylova, N.G., and Lyakhovitskiy, F.M., 1975, Low-frequency seismic waves in fluid-saturated layered rocks: Izvestija Academy of Science USSR, Physics of the Solid Earth, **10**, 654–659.

FIGURE CAPTIONS

Figure 1. Polar representation of energy velocities of qP and qSV waves of the 2PBM for a two-phase gas-water fluid mixture and those of the analytical model, the latter computed using and effective single phase fluids. Residual saturations are $S_{rn} = 0, S_{rw} = 0.01$.

Figure 2. Polar representation of attenuation coefficients of qP and qSV waves of the 2PBM for a two-phase gas-water fluid mixture and those of the analytical model, the latter computed using and effective single phase fluids. Residual saturations are $S_{rn} = 0, S_{rw} = 0.01$.

Figure 3. Polar representation of energy velocities of SH waves of the 2PBM for a two-phase gas-water fluid mixture and those of the analytical model, the latter computed using and effective single phase fluids. Residual saturations are $S_{rn} = 0, S_{rw} = 0.01$.

Figure 4. Phase velocity of “11” and “33” waves as function of frequency for the 2PBM for a two-phase gas-water fluid mixture and those of the analytical model, the latter computed using and effective single phase fluids. Residual saturations are $S_{rn} = 0, S_{rw} = 0.01$.

Figure 5. Attenuation coefficients of “11” and “33” waves as function of frequency for the 2PBM for a two-phase gas-water fluid and those of the analytical model, the latter computed using and effective single phase fluids. Residual saturations are $S_{rn} = 0, S_{rw} = 0.01$.

Figure 6. Polar representation of energy velocities of qP and qSV waves of the 2PBM for a two-phase gas-water fluid mixture and those of the analytical model, the latter computed using and effective single phase fluids. Residual saturations are $S_{rn} = 0., S_{rw} = 0.1$.

Figure 7. Polar representation attenuation coefficient of qP and qSV waves of the 2PBM for a two-phase gas-water fluid and those of the analytical model, the latter computed using and effective single phase fluids. Residual saturations are $S_{rn} = 0.$, $S_{rw} = 0.1$.

Figure 8. Patchy spatial distribution of nonwetting fluids. Nonwetting saturation values are $S_n = 0.012$ (black regions) , $S_n = 0.2$ (blue regions) and $S_n = 0.898$ (yellow regions). Overall nonwetting saturation is 10 %.

Figure 9. Polar representation of energy velocity of qP waves at 50 Hz for the 2PBM in the case of a fractured poroelastic medium with gas or oil saturation $S_n = 0.898$ in the fractures, $S_n = 0.012$ in the background versus patchy gas-brine and oil-brine saturation (Cases 1, 2, 3, 4). Overall nonwetting saturation is 10 %.

Figure 10. Polar representation of attenuation coefficient of qP waves at 50 Hz for the 2PBM in the case of a fractured poroelastic medium with gas or oil saturation $S_n = 0.898$ in the fractures, $S_n = 0.012$ in the background versus patchy gas-brine and oil-brine saturation (Cases 1, 2, 3, 4). Overall nonwetting saturation is 10 %.

Figure 11. Polar representation of energy velocity of qSV waves at 50 Hz for the 2PBM in the case of a fractured poroelastic medium with gas or oil saturation $S_n = 0.898$ in the fractures, $S_n = 0.012$ in the background versus patchy gas-brine and oil-brine saturation (Cases 1, 2, 3, 4). Overall nonwetting saturation is 10 %.

Figure 12. Polar representation of attenuation coefficient of qSV waves at 50 Hz for the 2PBM in the case of a fractured poroelastic medium with gas or oil saturation $S_n = 0.898$ in the fractures, $S_n = 0.012$ in the background versus patchy gas-brine and oil-brine saturation

(Cases 1, 2, 3, 4). Overall nonwetting saturation is 10 %.

Figure 13. Gradient of total fluid pressure $\|\nabla\tilde{\mathcal{T}}\|$ at 50 Hz for the 2PBM and compression normal to the fractures (p_{33} -experiment). Overall patchy gas-brine saturation is 10 %.

Figure 14. Gradient of total fluid pressure $\|\nabla\tilde{\mathcal{T}}\|$ at 50 Hz for the 2PBM and compression normal to the fractures (p_{33} -experiment). Overall patchy oil-brine saturation is 10 %.

FIGURES

LIST OF FIGURES

- 1
- 2
- 3
- 4
- 5
- 6
- 7
- 8
- 9
- 10
- 11
- 12
- 13
- 14

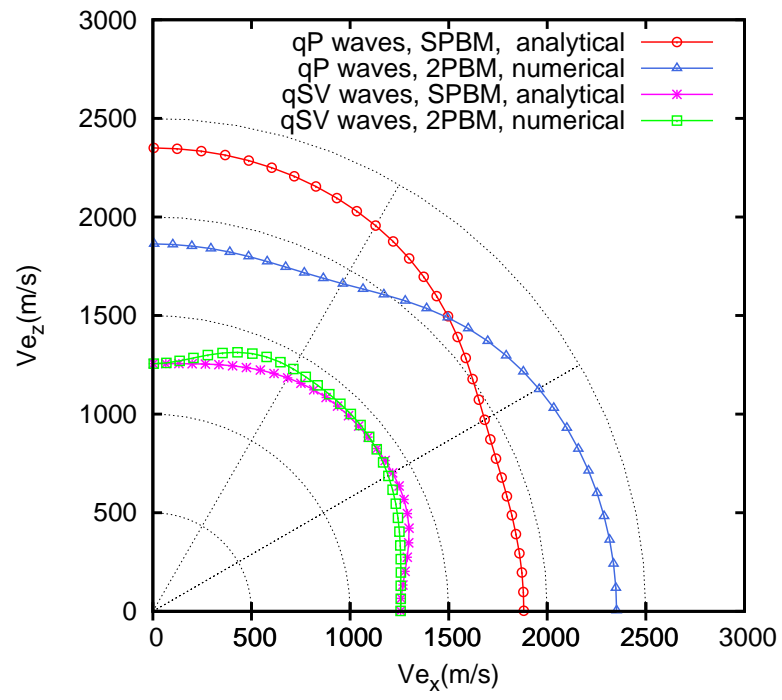


Figure 1: Santos –

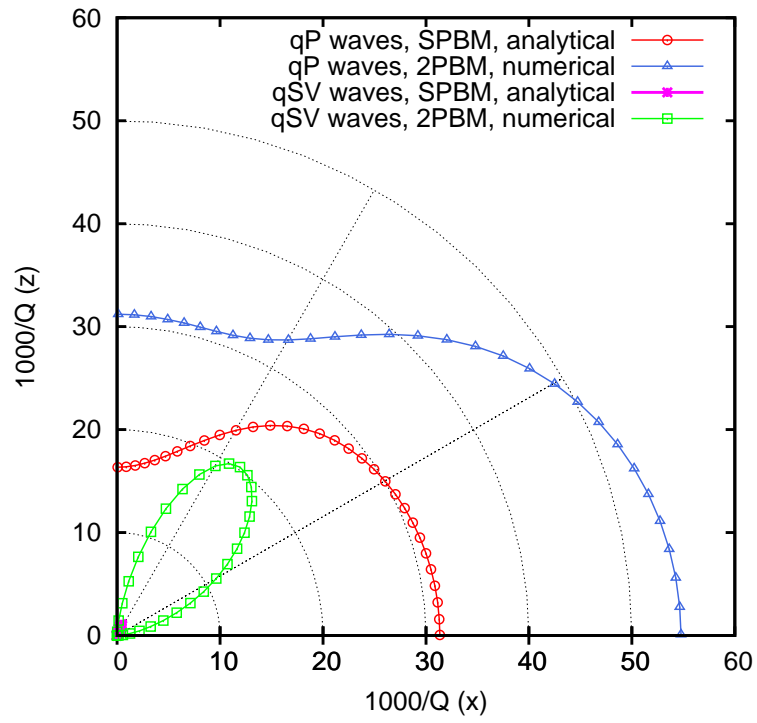


Figure 2: Santos –

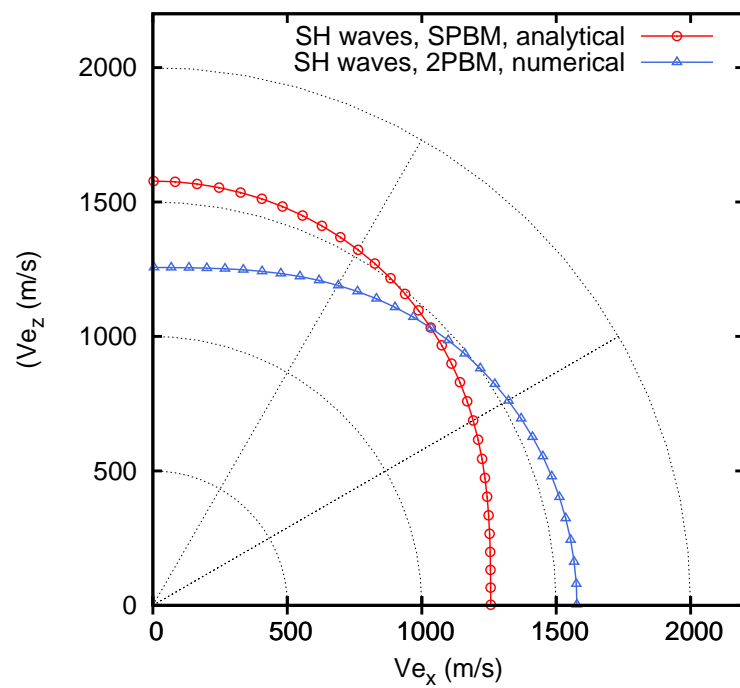


Figure 3: Santos –

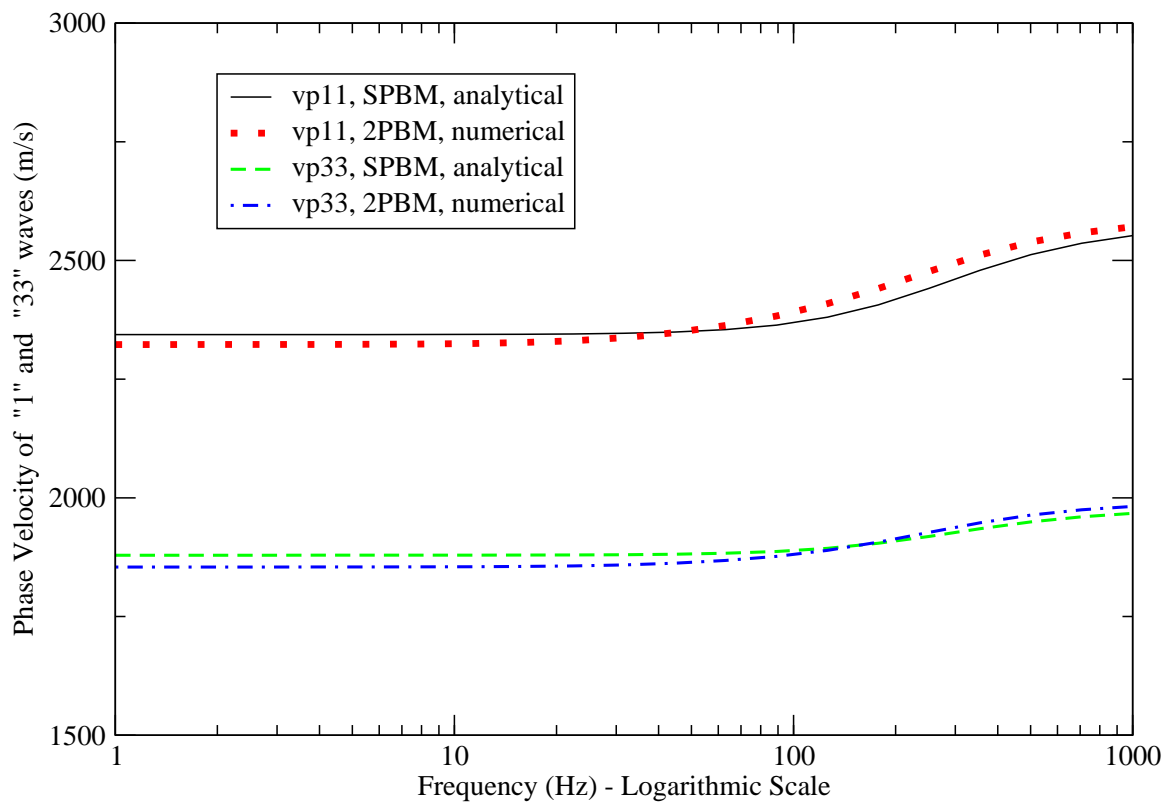


Figure 4: Santos –

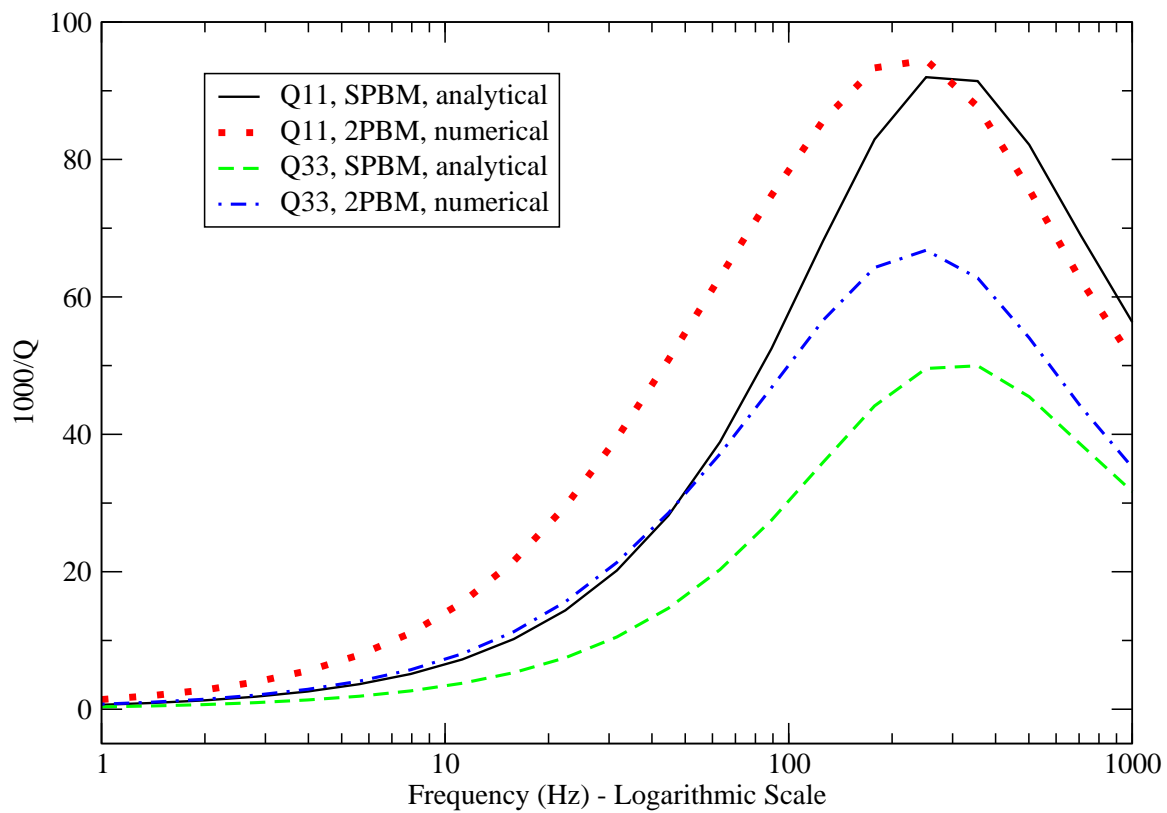


Figure 5: Santos –

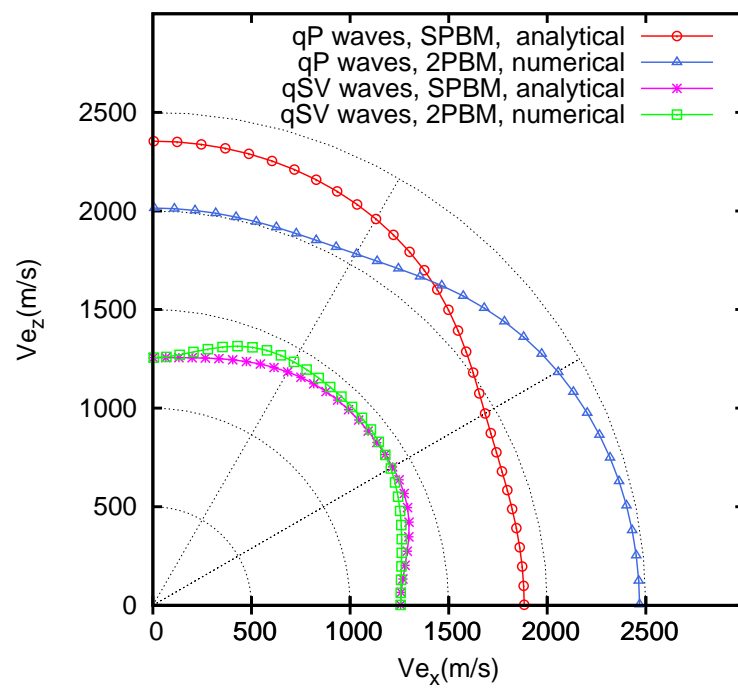


Figure 6: Santos –

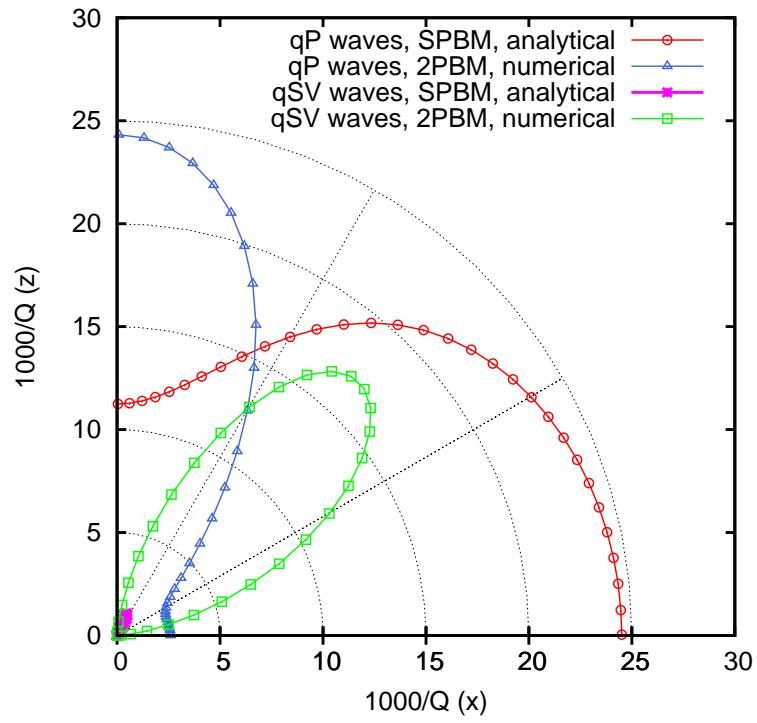


Figure 7: Santos –

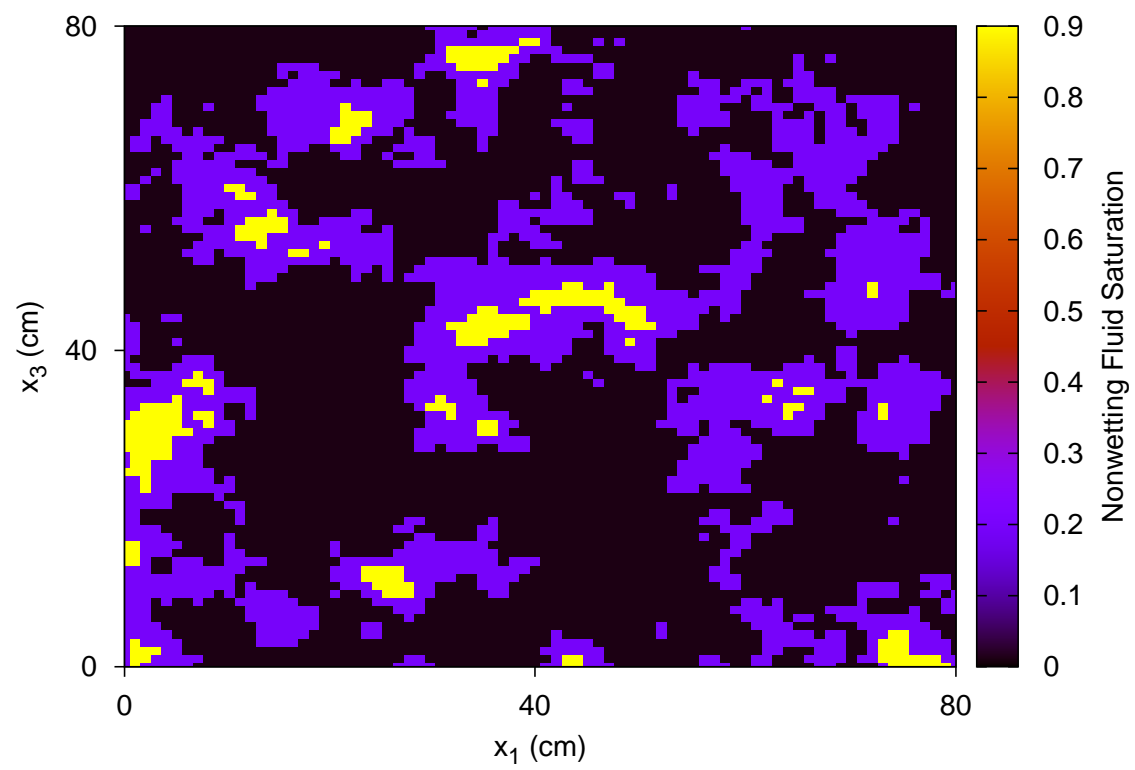


Figure 8:Santos –

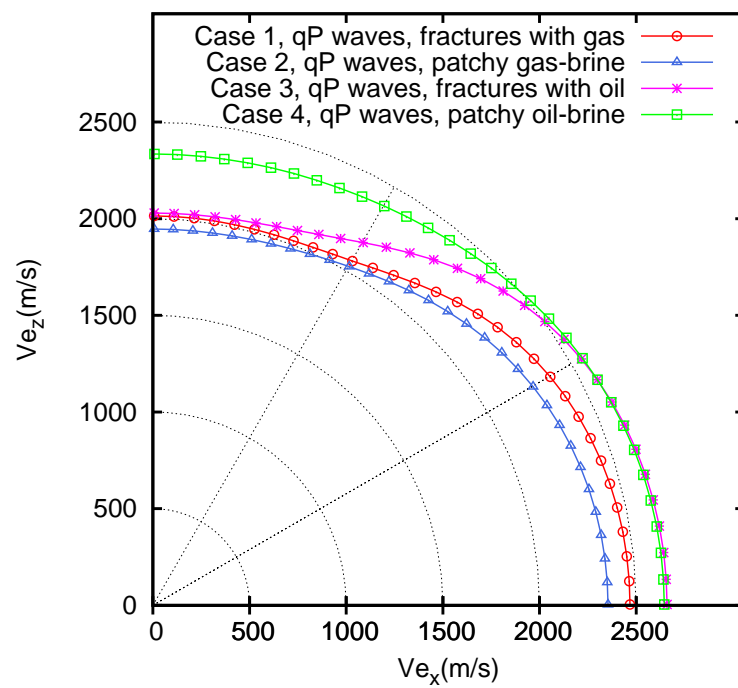


Figure 9: Santos –

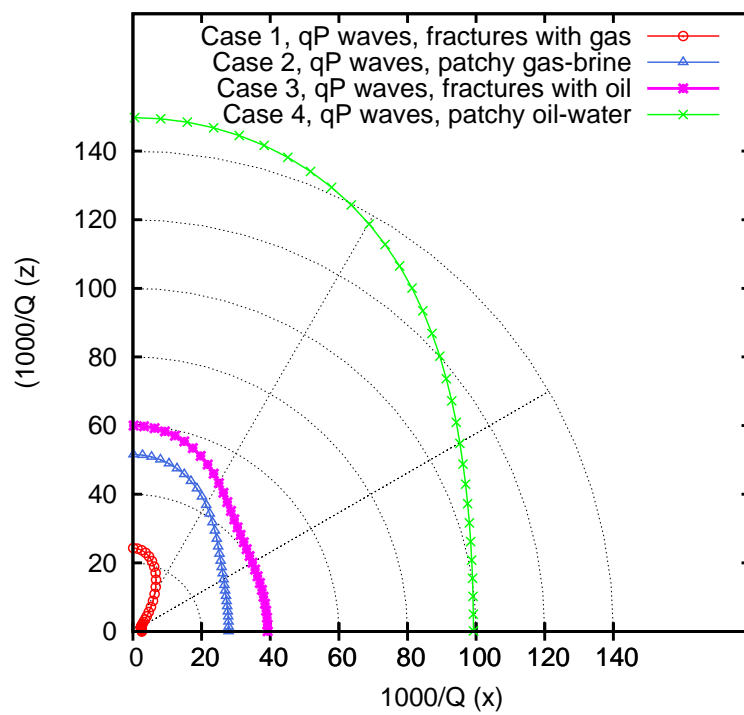


Figure 10:Santos –

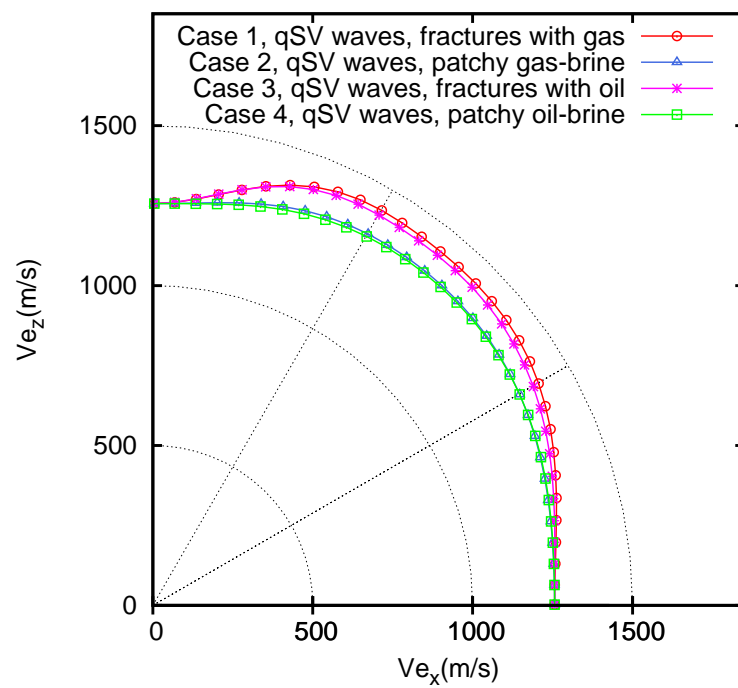


Figure 11: Santos –

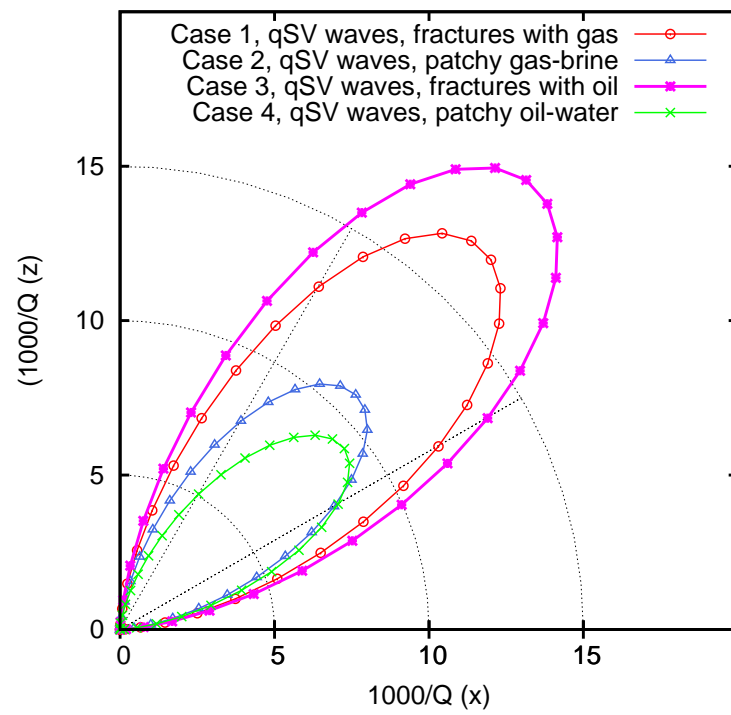


Figure 12: Santos –

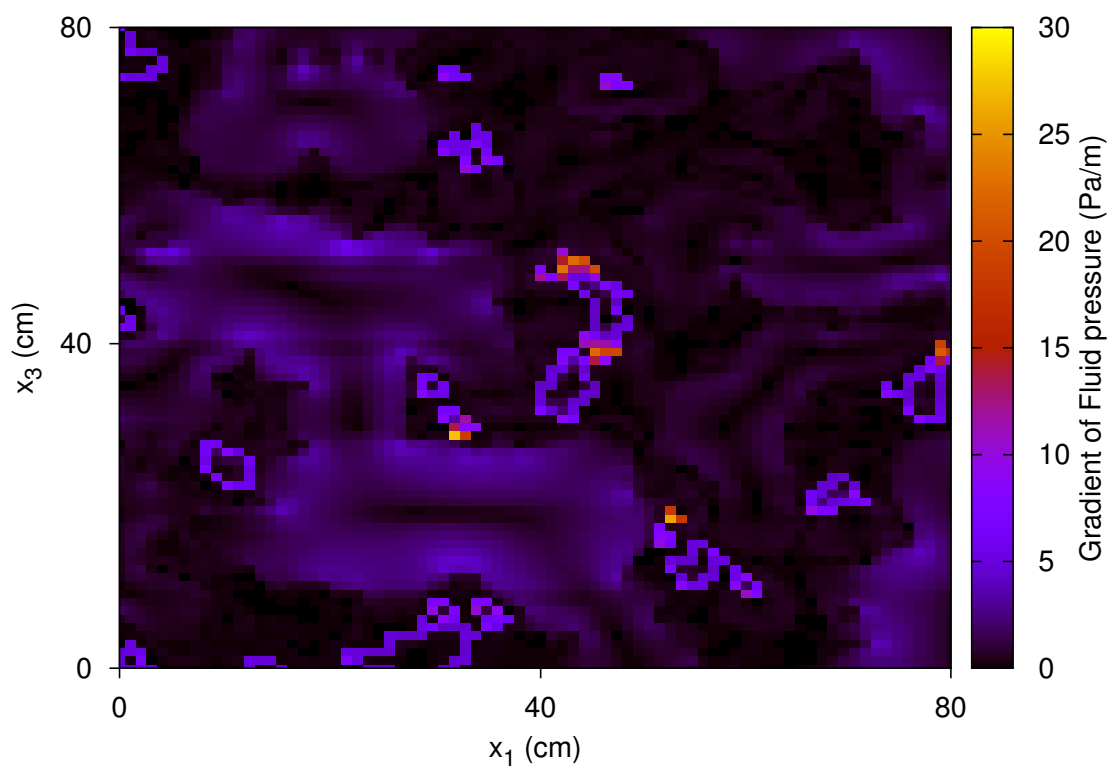


Figure 13: Santos –

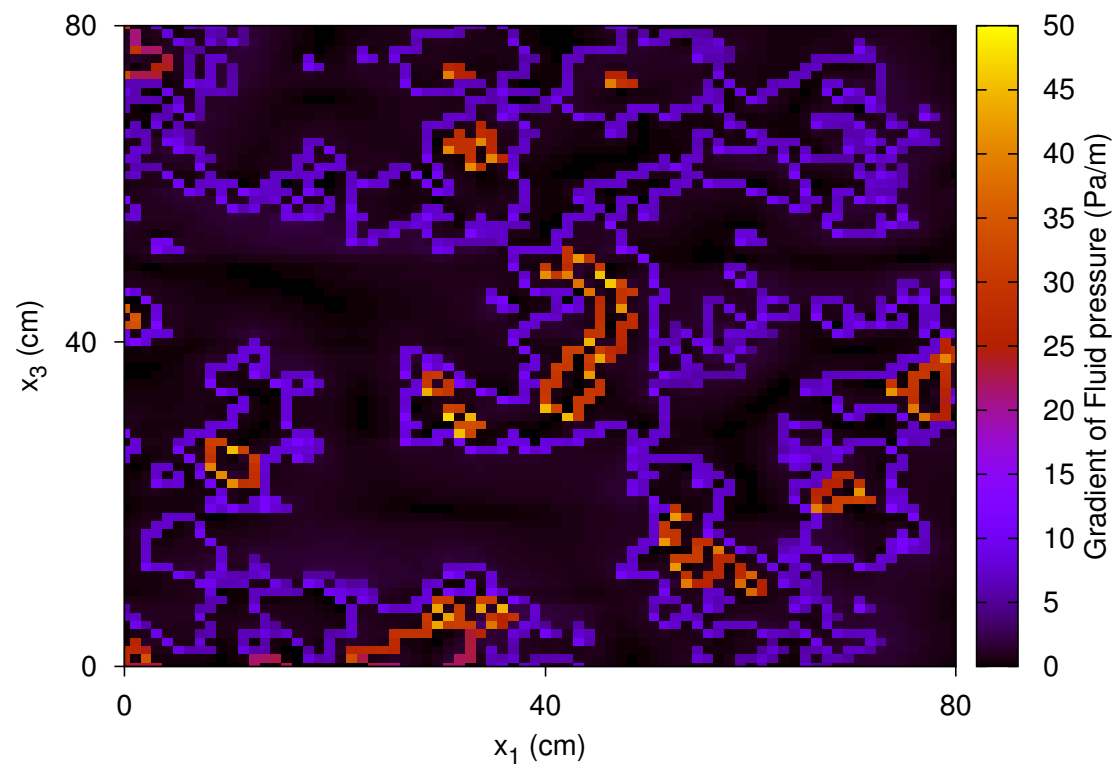


Figure 14: Santos –